TiO_2 Nanofilms on Polymeric Substrates for the Photocatalytic Degradation of Methylene Blue

Hesam Maleki[†] and Volfango Bertola[*,†,‡]

[†]*School of Engineering, University of Liverpool, Liverpool*

[‡]*Current address: Liverpool, United Kingdom, L69 3BX*

E-mail: Volfango.Bertola@liverpool.ac.uk

Phone: +44 (0)151 794 4804

Abstract

A low-temperature process to synthesize and print photoactive TiO_2 nanofilms onto polymeric substrates using a modified desktop inkjet printer is presented. The coated substrates were assembled in a microfluidic device for photocatalytic studies fabricated by selective transmission laser welding. The synthesized TiO_2 showed a competitive activity compared with commercial TiO_2 nanopowders. Furthermore, the coated catalyst remained active and intact even after a long-term reaction run. The inkjet printing method can be utilized for the efficient immobilization of catalytic films onto reactor walls in the design of continuous flow reactors. A dispersed TiO_2 sol was prepared by the thermohydrolysis of $TiCl_4$ below 100°C. The resulting sol was stabilized using ethylene glycol and directly printed onto the substrate without further heat processing. The printability and colloidal stability of the inks were assessed by measuring their rheological and interfacial properties. X-ray Powder Diffraction (XRD) analysis identified the synthesized TiO_2 as pure anatase nano-sized particles ($\sim$ 4.5 nm) verified by transmission electron microscopy (TEM). The photocatalytic activity of the printed layers was studied in the microreactor based on the degradation of

methylene blue. Inkjet printing proved to be a customizable technique for coating active nanocatalysts. The overall process presented here is cost-effective and efficient in manufacturing flexible lightweight microreactors coated with highly tunable TiO_2 catalytic films.

Keywords: photocatalytic activity, microreactor, inkjet printing, TiO_2, anatase, low temperature process.

1 Introduction

Photocatalysis is a developing branch of heterogeneous catalysis with numerous applications mainly in air and water pollutant treatment.[1,2] This technology is considerably effective in removing different types of contaminants compared to conventional treatment methods such as ozonolysis and chlorination.[3,4] In photocatalytic reactions, UV/visible light absorption generates pairs of electron-hole on the surface of the catalyst. The oxygen and water molecules in the media react with the excited electrons and holes which create oxide ($\cdot O_2^{-1}$) and hydroxyl ($\cdot OH$) radicals, respectively. These radical species play a key role in photocatalytic oxidation reactions.[5]

TiO_2 and TiO_2-based semiconductors are considered to be the first choice of photocatalysts among other alternatives because of their low cost, chemical compatibility, high stability and significant oxidizing activity.[6,7] Among the different crystalline phases of titanium dioxide, anatase and rutile phases have gained more attention due to their lower recombination rate of generated electron-hole pairs leading to higher photocatalytic performance.[8,9] Chemical and physical properties of TiO_2 can be manipulated easily using different synthesis and post-synthesis methods. Therefore, various approaches have been proposed to tailor high photoactive TiO_2 catalysts. Preparing TiO_2 particles using hydrothermal and sol-gel methods, and altering the morphology, crystallinity and surface area of the samples are typical methods.[5,10,11]

Generally, photocatalytic processes take place in batch agitated reactors using dispersed

catalytic particles. This method suffers from particle agglomeration as well as photon transfer resistance from the external source into the reaction media. Furthermore, dispersed catalysts must be filtered in downstream or from the reactor medium after each cycle.[12] Many attempts have been made to fix the photocatalytic particles in continuous reactor systems such as using optofluidic devices or coated microchannels manufactured on ceramics, glass or silicon.[13,14] Despite the significant progress of coating techniques in macro and microfluidic devices, there are still limitations due to complex fabrication procedures and low performance.[15] Conventional deposition methods such as dip-coating and spin-coating suffer from producing large waste of materials and low capability in patterning and film thickness control.[16] Other alternatives like lithography and vacuum deposition involve costly multi-step processing at elevated temperatures.[17]

Among different coating techniques, inkjet printing is rapidly gaining momentum and was proved suitable for non-contact uniform coating of functional metal oxides such as TiO_2.[18–20] The dominant method of choice in inkjet printing is drop-on-demand (DOD) mode.[17,21] In DOD mode, materials in the form of inks can be printed on the substrate through thermal or piezoelectric printheads without further processing.[21,22] The ink must be specially formulated to be printable and thereby transferring the functional ingredients onto the substrate effectively. Complex patterns can be readily printed using inkjet printing. The layer thickness is adjustable and the waste of material is minimum.[23]

Viscosity and surface tension are the key properties to characterize jettable inks for inkjet printing applications. The recommended viscosity range for DOD printers is 1 to 25 mPa·s.[24] At higher viscosities, ink droplets cannot jet properly from the nozzle at specified rates. At the same time, low viscosities create unstable droplets during printing leading to the formation of satellite droplets. The recommended range for surface tension is 20 to 50 mN/m. Lower surface tensions would cause air-ingestion and dripping of droplets.[25]

Whilst viscosity, surface tension and density are necessary to characterize the droplet formation, the printability also depends on the nozzle diameter and jetting conditions. These

parameters are combined in the Weber number, $We = \rho v^2 d/\gamma$, and the Reynolds number, $Re = \rho v d/\eta$, where γ is the surface tension, ρ the density, η the dynamic viscosity of the fluid, d is the nozzle diameter and v the fluid velocity. These dimensionless numbers are often merged into a single parameter, the inverse Ohnesorge number, $Oh^{-1} = Re/\sqrt{We} = \sqrt{\gamma \rho d}/\eta$, which is commonly used to characterize the ink printability.[26,27] Ink droplets are printable in a DOD system when $1 < Oh^{-1} < 10$.[28]

Inkjet printing was recently used to manufacture sensors[29,30] and other electronic devices such as solar cells,[31] transistors[32] and supercapacitors.[33,34] However, applications of inkjet printing in catalysis systems are scarce, and usually consist of printing a catalyst onto glass substrates, followed by thermal treatment.[35–39] Černá et al.[5] prepared TiO_2 nanopowders using the hydrothermal method under acidic conditions. The formulated colloidal ink was printed on soda-lime glass and sintered at 500°C for photocatalytic assessments. A chemical solution deposition approach was studied by Arin et al.[40] to inkjet print TiO_2 layers on glass substrates starting from a titanium alkoxide precursor. After printing, samples were sintered at 500-650°C and the photodegradation tests were performed on methyl orange. There have been reports in the literature on the deposition of functional TiO_2 films at low temperatures.[41,42] Low-temperature deposition would open a large market for coating thermo-sensitive materials. Furthermore, it would extend the use of polymers as coating substrate as a competitive sustainable alternative.[43]

This work investigates the photocatalytic activity of inkjet-printed TiO_2 layers on polymeric substrates in a microfluidic device. Photoactive TiO_2 nanopowders were synthesized through a calcination-free route. Inks were prepared directly from the synthesized TiO_2 sol and used in a modified commercial printer. The printed substrates were then employed as channel walls in a microreactor manufactured by selective transmission laser welding. The photocatalytic degradation of methylene blue in the microfluidic device was studied under different reaction conditions. The overall characterization and kinetic studies were performed on the synthesized TiO_2 and commercial TiO_2 nanopowders.

2 Experimental

2.1 TiO_2 synthesis

Titanium(IV) chloride ($TiCl_4$, 99.9%, ACROS Organics) was added dropwise to deionized water ($TiCl_4/H_2O$ volume ratio: 1:10) in an ice-water bath inside an argon purged glove box. After continuous stirring for 12 h at room temperature, the transparent sol was diluted with a mixture of water, and the $TiCl_4/H_2O$ volume ratio of 1:60 was prepared. The resulting solution was boiled three times with consecutive sonication in a 60 min boiling plus 15 min sonication cycle. Finally, most of the HCl gas generated was removed during the boiling/sonication process, and suspended TiO_2 particles were obtained. NaOH (Sodium Hydroxide, 1N, Fisher Chemical) was added to the sol to increase the pH above 7 and ease the washing process. The dispersed solution was then washed several times with water to remove the remaining chloride ions and to reach neutral pH. The aqueous dispersed TiO_2 sol was directly used in the ink formulation without additional treatments. For powder characterization studies, the dispersed particles were dried at 80°C overnight.

2.2 Ink preparation

TiO_2 was added to pure ethylene glycol (EG, 99%, Alfa Aesar) in form of dry powder or sol product of synthesis. A small volume of HCl (Hydrochloric Acid Solution, 1M, Fisher Chemical) was added to maintain the pH around 4. The as-prepared ink was used to disperse the TiO_2 samples: synthesized TiO_2 sol (T-sol) and a commercial mixture of rutile and anatase (Titanium(IV) oxide, 99.9%, Sigma-Aldrich) (T-sig). The final TiO_2 concentration in the inks was set to 0.5 wt%. The formulated inks were stirred thoroughly and sonicated for 30 minutes at 50°C. The dispersion medium was filtered through a 0.8 μm hydrophobic syringe filter and inserted directly into the printer ink tank.

2.3 Inkjet printing

Inkjet printing was performed using an affordable Epson XP-335 printer with minor modifications similar to the procedure described by Waasdorp et al..[25] A continuous ink system (CIS) was connected to the printer to ease the refilling process using external ink tanks. Following their procedure, half-size A4 paper sheets (100 mm × 297 mm) were placed on the right side of the printer tray to ensure smooth operation of the printer, while the substrate was placed in the other half, under the printhead (see Figure S1). The printer was configured to the default colour setting. A polypropylene sheet (Kitronik Ltd, 0.4 mm thickness) was selected as printing substrate. Polypropylene is a low-cost, flexible and recyclable material which is resistant to abrasion and acidic/alkaline solutions with the thermal stability up to 130°C.[44] Prior to printing, transparent polypropylene sheets were rinsed with deionized water and ethanol (C_2H_6O, 99.8%, Fisher Chemical). To increase the polymer surface energy and consequently improve printing, oxygen plasma treatment (Henniker Plasma, HPT-100) was applied over the substrates for 5 min at 100 W power to activate the surface and enhance the adhesion. Subsequently, the TiO_2 ink samples were printed on the treated substrates and reprinted for different layer numbers after consecutive dryings at 100°C. The printed substrates with different TiO_2 contents were used in the fabrication process and photocatalytic experiments without further activation as shown in Figure 1.

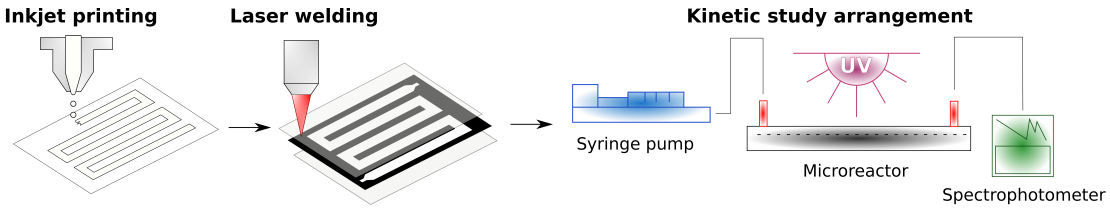

Figure 1: Schematic illustration of the inkjet printing, microreactor fabrication and photocatalytic study set-up.

2.4 Fabrication of the microreactors

The microreactor structure consists of a serpentine channel cut-out in a sheet of black polypropylene placed between two transparent sheets of the same polymer welded on both sides by selective transmission laser welding. Figure 1 indicates a schematic diagram of the process. In selective laser transmission welding, the laser photons are transmitted through the transparent layer and absorbed by the adjoining black layer. Absorption of energy melts the interface zone uniformly and welds the two polymeric parts.[45,46] The 2D geometry of the serpentine channels was designed in Creo Parametric 5.0 and sent to an LS1290 PRO Laser Cutter (power: 80 W; cutting area: 120 cm × 90 cm). The cutting was performed with repeating engraving passes on the polypropylene sheets to improve the finish. Afterwards, the surface of the cut parts was rinsed with ethanol to remove debris. To ensure uniform and seamless welding, the polypropylene sheets were clamped between a 6 mm thick glass plate and a 3 mm thick aluminium plate. Welding was then carried out using a nanosecond pulsed fibre laser (SPI G4 HS-L 20 W) with a wavelength of 1064 nm. The irradiation on polymeric sheets had a pulse repetition rate of 500 kHz and a spot size of 45 μm, while the laser power was set to 20 W and the scanning speed to 18 mm/s. The fabricated microreactor with 8 mm (width) × 0.7 mm (depth) channel dimensions and overall volume of 2.5 cm^3 is shown schematically in Figure 2.

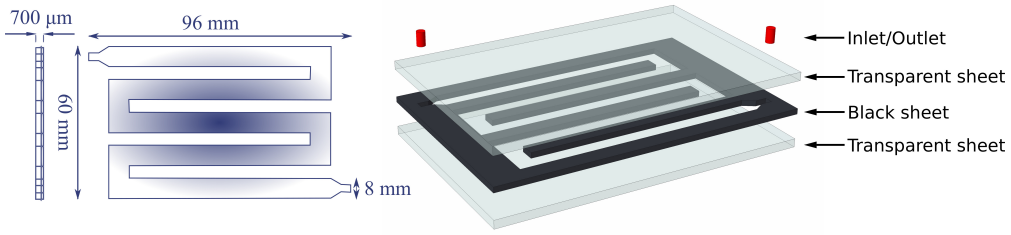

Figure 2: Drawing of the manufactured microreactor with specified dimensions.

2.5 Characterization

TiO_2 photocatalyst samples were analysed for crystallinity with X-ray diffraction (XRD) technique. A Rigaku MiniFlex 600 diffractometer was used for characterization with CuKα as the radiation source at 30 kV/15 mA. The data were collected from 20°to 70°(2θ) with a step interval of 0.1°. The phase analysis of the samples was performed with reference to the XRD patterns from Crystallography Open Database (COD). The solid samples were dried at 100°C for 1 h before analysis. The particle size was calculated using Scherrer's equation:[47]

$$d = \frac{B \cdot \lambda}{\beta \cdot cos\theta} \tag{1}$$

where B=0.94 is a constant value (dimensionless shape factor), λ is the X-ray wavelength which equals 0.154 nm, and β is the peak width at half of the maximum intensity. The morphology of TiO_2 nanostructures was characterized using a scanning electron microscope (JEOL JSM-7001F) operated at 5 kV. Dried samples were simply coated onto carbon adhesive discs for SEM analysis. For higher resolution images, a JEM-2100 Transmission Electron Microscope was used equipped with a LaB_6 (lanthanum hexaboride) filament operating at 200 kV. The particle size distribution was measured using dynamic light scattering (DLS) with a Zetasizer Nano ZS (Malvern Instruments, UK). Data were recorded at 25°C and wavelength of 633 nm. The Wilhelmy plate method was used to calculate the surface tension of TiO_2 ink samples using a Krss K20 EasyDyne Tensiometer. In this method, a suspended plate is in contact with the liquid surface vertically, and the surface tension can be measured directly from the created force and the wetted length. The surface tension for each sample was measured 3 times. The ink dynamic viscosity was evaluated with an Anton Paar MCR302 rheometer at 25°C. The loading mass of printed TiO_2 on the substrate was determined by a simple gravimetric method. The weight of the substrate was measured before printing and then after the printing and drying procedure. The calculated weight values were compared with the weight measurements based on the mean volume of the jetted ink

microdroplets. Uniformity and structure of the printed TiO_2 on the microchannel walls were observed using optical microscopy (Nikon Eclipse LV150NL microscope) and SEM.

2.6 Photocatalytic experiments

Photocatalytic experiments were carried out in the microreactor at atmospheric pressure and ambient temperature. T-sol and T-sig samples were used in the experiments as well as a commercial TiO_2 (Evonik Aeroxide P-25) as a comparative standard. A diluted aqueous solution of methylene blue (MB, Alfa Aesar) was selected for the photocatalytic reaction with an initial concentration of 1.25×10^{-5} mol·L^{-1} (4 ppm) at inlet. UV light was illuminated from a 9 W UVP Compact UV Lamp at 368 nm. A syringe pump (Razel A-99) was used to drive the initial MB solution into the microreactor through the inlet at different flow rates. The reaction products were collected from the outlet at different time intervals and analysed with a Spectronic 200 Spectrophotometer. The sample analysis was delayed for 2 h after the process initiation to allow the catalyst layer to reach the adsorption-desorption equilibrium and the reactor setup to reach the steady-state condition. For the batch reactor analysis, the reaction occurred in a beaker agitated with a magnetic stirrer. The same MB concentration was used with 0.1 g of TiO_2 per 100 ml of reaction volume. Samples were taken at regular time intervals for the conversion measurements. Before the activity studies, the reaction was kept in the dark for 60 min to reach the equilibrium state. The methylene blue conversion rates were measured from the absorbance analysis for the kinetic study. According to Beer-Lambert law, the absorbance is proportional to the concentrations ($C \propto A$); thus, the conversion can be defined as:

$$X_{MB} = 1 - \frac{C_{MB}}{C_{MB0}} = 1 - \frac{A}{A_0} \tag{2}$$

where X_{MB} is the conversion of methylene blue in the reaction which is related to the absorbance ratio of the product to the initial value (A/A_0).

3 Results and discussion

3.1 Powder characterization

X-ray diffraction spectra of TiO_2 samples are shown in Figure 3. The structure of peaks for the synthesized sample (T-sol) confirms the dominance of partially crystallized phase of anatase. The XRD pattern indicates five broad peaks corresponding to the (101), (103, 004, 112), (200), (105, 211) and (204) reflection of anatase, respectively. The broad form of the peaks is probably due to the small particle size. The crystalline size was estimated from the (101) peak width using the Scherrer equation. The commercial TiO_2 (T-sig) exhibits sharp peaks of anatase (labelled A) and rutile (labelled R) with an average crystalline size of 33 nm. The crystalline properties of the examined TiO_2 powders are listed in Table 1.

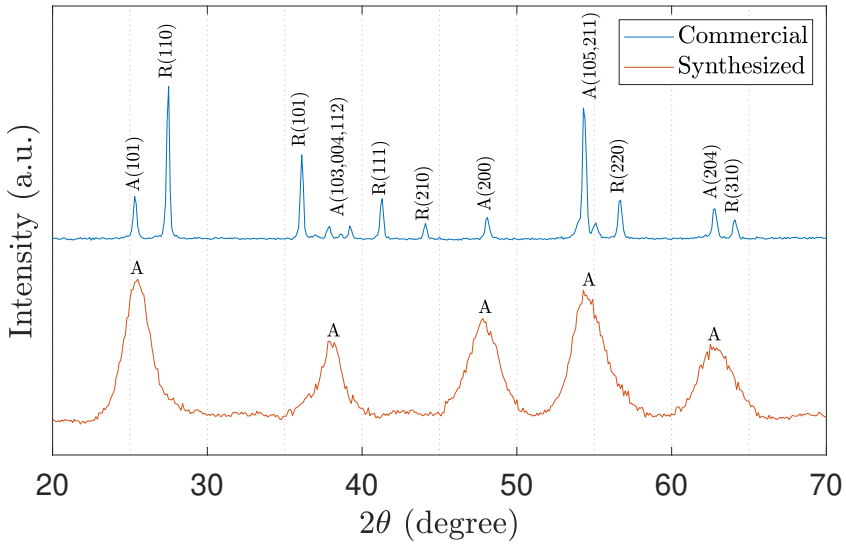

Figure 3: XRD diffraction spectra of TiO_2 dry samples: TiO_2 obtained by thermohydrolysis and commercial T-sig nanopowders. (hkl) indices are given for the anatase (labelled A) and rutile (labelled R) phases.

Selected SEM and TEM images of the catalyst powders are given in Figure 4. The T-sig sample presents primary small crystallites and larger secondary ones due to particle agglomeration.[48] Differentiating between the anatase and rutile phases in the commercial sample

is difficult due to similar qualitative morphologies. The texture of the synthesized sample consists of tiny particles interlaced with each other forming densely packed nanostructures.

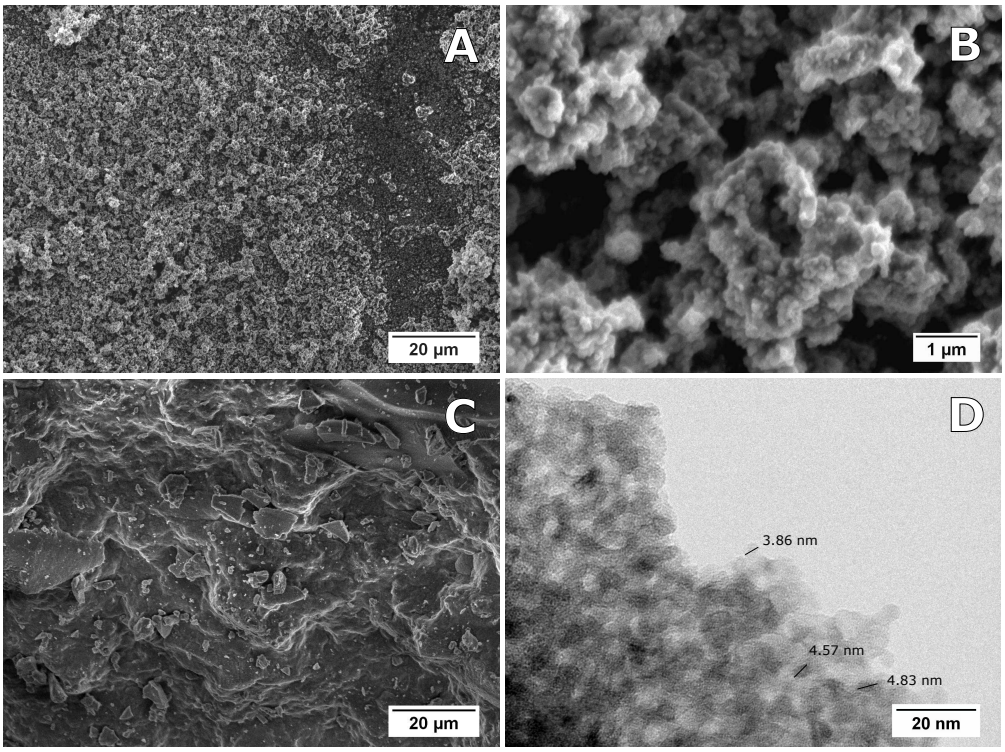

Figure 4: SEM images and TEM image (D) of TiO_2 dry samples: T-sig (A, B) and synthesized TiO_2 nanopowders (C, D) with different magnifications.

Table 1: Crystalline properties and photocatalytic activity of TiO_2 catalysts.

Catalyst	Crystal phase[a] (% vol.)	XRD size (nm)	k (min^{-1})[b]
T-sol	A (100%)	4.2	0.021
T-sig	A (52%)/R (48%)	31[A], 38[R]	0.012
P-25	A (80%)/R (20%)[48]	25[A], 33[R][48]	0.028

[a] Crystal phase ratio was measured based on the method reported by Xianzhi et al..
[b] Rate constants were measured in the batch reactor containing 0.1 g catalyst (see Figure S2).

3.2 Ink characterization

The TiO_2 inks were carefully modified and optimised with altering solution formulations (see Table S1). The measured viscosity and surface tension of prepared inks are listed in Table 2.

Ethylene glycol was added to the ink solution as the dispersing agent to optimize the viscosity and hinder the air intake at the nozzle, resulting in creating stable drops during the printing procedure. EG is frequently used in the design of inks and paints.[50] Existence of secondary micron-sized particles in agglomerate forms limits the application of inks for inkjet printing due to the nozzle blockage at the beginning of printing. Thus, a small volume of dilute HCl was used in the dispersed solutions to create a repulsive effect by charge generation. The weak acidic environment prevents the particles from producing agglomerates.[51] The dispersed nanoparticles smaller than 1/50 of nozzle diameter can pass smoothly through the printer nozzles.[52]

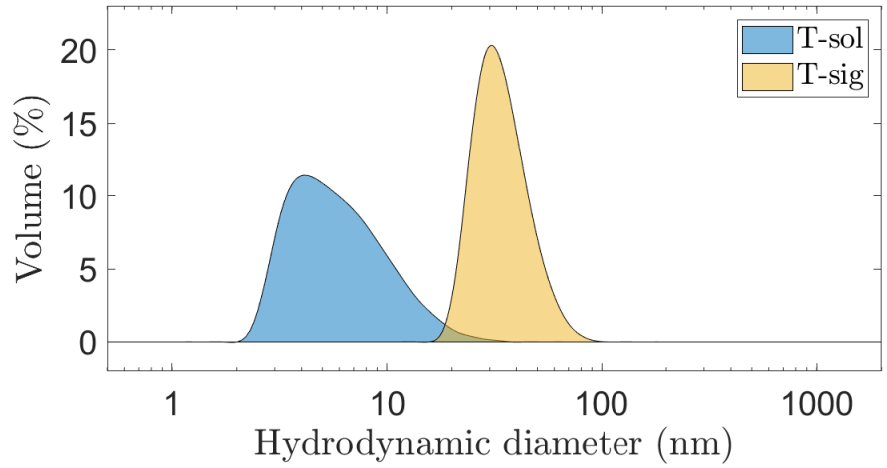

Figure 5: Hydrodynamic size distributions of TiO_2 colloidal inks obtained by DLS containing T-sol and T-sig.

Figure 5 shows the hydrodynamic size distribution of dispersed TiO_2 particles in EG-based inks. The distribution of TiO_2 colloids is unimodal in both samples, and particles are stabilized at values under 100 nm. These size ranges ensure that the agglomerates are tiny enough to pass through the nozzles without any clogging. The dispersed particles in the prepared solutions were stable during the first hours of usage. Some sedimentation was observed in the ink solution containing T-sig after 7 days of storage. However, the T-sol ink showed long-term stability without significant particle sedimentation (see Figure S3). The T-sol particles are smaller in size, and the ink was prepared directly from the TiO_2 sol which

may cause the higher colloidal stability.

3.3 Printability

The formulated inks fall within the range of 1< Oh^{-1} <10, i.e., they are suitable for the printing process. High wettability occurs for the liquids with a surface tension lower than the surface free energy of the substrate. Hence, water-based inks ($\gamma_{lg} \approx 70$ mN/m) may not be printed effectively on polymeric substrates (γ_{sg} = 20-50 mN/m) due to partial/poor wetting. However, plasma-treated polymeric surfaces have higher surface free energies, and the prepared EG-based inks showed higher wettability and maintained lower drop contact angles on the treated polypropylene substrates (see Figure S4).

Table 2: Fluid properties and formulation of colloidal inks at 25°C.

Ink	Material	Dynamic viscosity (mPa.s)	Surface tension (mN/m)	Z (Oh^{-1})[a]	d_H (nm)[b]
1	T-sol (TiO_2: 0.5 wt%) HCl (0.005 M) Ethylene glycol	8.6 ± 0.1	50.3 ± 0.3	3.8	8.3
2	T-sig (TiO_2: 0.5 wt%) HCl (0.005 M) Ethylene glycol	13.4 ± 0.1	48.4 ± 0.2	2.4	64.4

[a] The nozzle diameter is approximately 20 μm for the Epson XP Series.
[b] The intensity weighted mean hydrodynamic diameter of prepared inks measured by DLS.

A general view of individually printed droplets and loaded catalyst layer is shown in Figure 6. The single droplet size is in the range of 20-50 μm but may vary depending on the printer setting, the ink formulation, and the surface properties. On hydrophobic surfaces, droplets are smaller in diameter.[25] As confirmed by optical microscopy and SEM image of printed samples, nanopowders are uniformly printed on the polypropylene substrate. Compared to lab-scale printing platforms and microdrop dispensers, desktop inkjet printers create smaller droplets with higher dispensing rates due to higher number of nozzles with smaller diameter size.

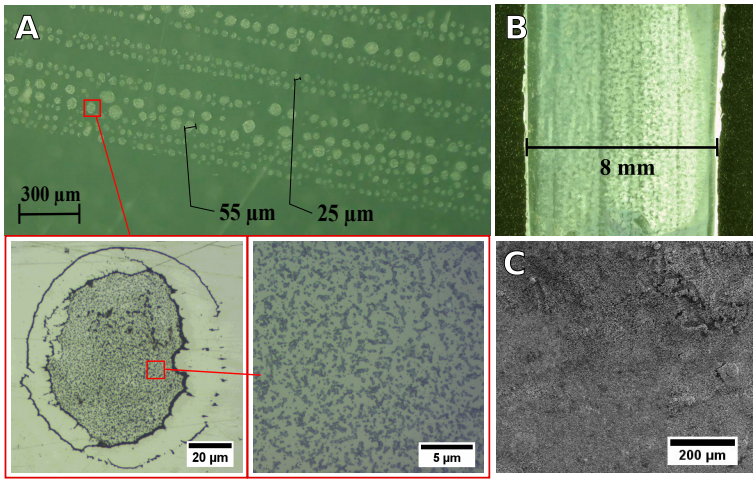

Figure 6: Individual dried droplets of prepared T-sol ink on polypropylene substrate (A). One and two print passes. Printing was continued to make a layer with a specific TiO_2 weight (B, C).

3.4 Photocatalytic study

The photodegradation reaction was studied on a methylene blue solution as a standard dye with an initial concentration of 4 ppm. At this order of concentration, the MB solution is visible and easily detectable by spectrophotometry with low absorptions at 360-400 nm wavelengths. Moreover, the process operates under kinetic control with low mass transfer limitations. Figure 7 shows the absorption spectra of the methylene blue solution during a typical reaction operation under UV illumination. As the reaction proceeds, the absorbance decreases with time with maximum peak values at the wavelength of 667 nm. According to literature, MB reacts with generated (·OH) radicals and breaks into compounds with shorter absorption wavelengths including CO_2 and H_2O.[53]

The MB conversion curve of photodegradation reaction versus the residence time is given in Figure 8 for different reaction conditions. The graphs show exponential trends for both samples following the pseudo first order kinetics within the examined range as described by the following equation:

$$ln(1 - X_{MB}) = ln(\frac{C_{MB}}{C_{MB0}}) = -kt \tag{3}$$

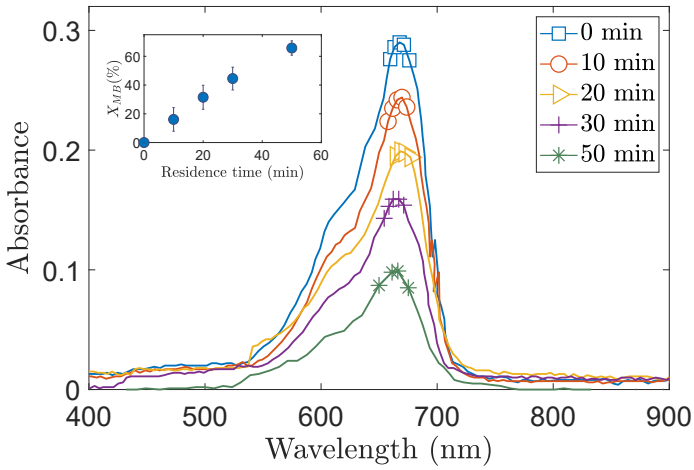

Figure 7: Absorption spectra of MB during 50 min of photodegradation in the batch reactor containing 0.1 g of T-sol catalyst (reaction volume: 100 ml; C_{MB0}: 4 ppm).

where X_{MB} is the conversion of methylene blue after the reaction residence time t, C_{MB0} is the initial concentration of MB, and k is the apparent reaction rate constant. The synthesized TiO_2 showed higher activity in comparison with T-sig sample. This may be due to the smaller particle size of T-sol sample observed by TEM analysis. Lower particle size creates a higher active surface area of the catalyst medium resulting in higher photocatalytic activity. Furthermore, T-sol sample has anatase crystal structure which has been reported to show more activity in photocatalysis.[3,54,55] However, the T-sol activity is lower than that of commercial P-25 in the reaction. Because lack of calcination during the T-sol synthesis would probably result in lower crystallinity.

As shown in Figure 8, increasing the TiO_2 layers enhanced the activity of the photodegradation reaction. The enhancement in activity is a consequence of the increase in the number of catalytic active sites. Nevertheless, the additional layer did not exhibit the same activity as the first layer of the printed TiO_2 on the substrate. This may be caused by the limitation of photon transfer due to the self-shadowing effect[5] or mass transfer resistance for the MB molecules at deeper layers of the catalyst.

Finally, a stability test was performed over the microreactor coated with T-sol at 1 ml/h flow rate (see Figure 9). For a 48 h continuous run, nearly constant conversion values were

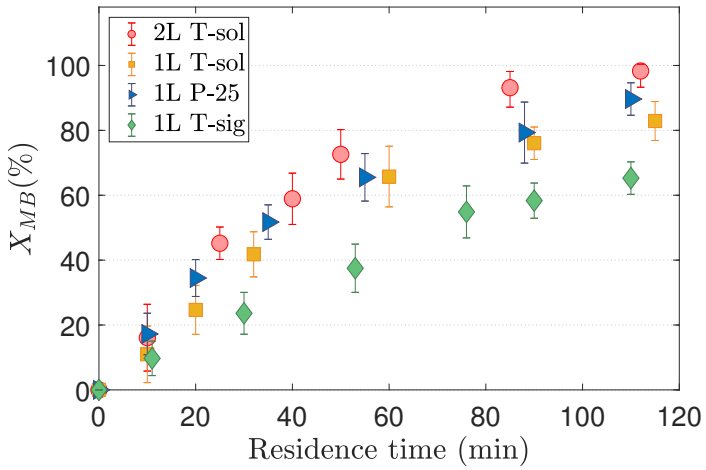

Figure 8: Photocatalytic degradation of methylene blue as a function of residence time: 2 layers of T-sol; 1 layer of T-sol; 1 layer of Degussa P-25 and 1 layer of T-sig catalysts (1 layer: 0.035 mg/cm^2 of TiO_2; C_{MB0}: 4 ppm).

recorded. Moreover, no TiO_2 sedimentation was observed from the samples taken from the outlet. This confirms the stability of the fixed printed catalyst layers on the microreactor walls under mild reaction conditions.

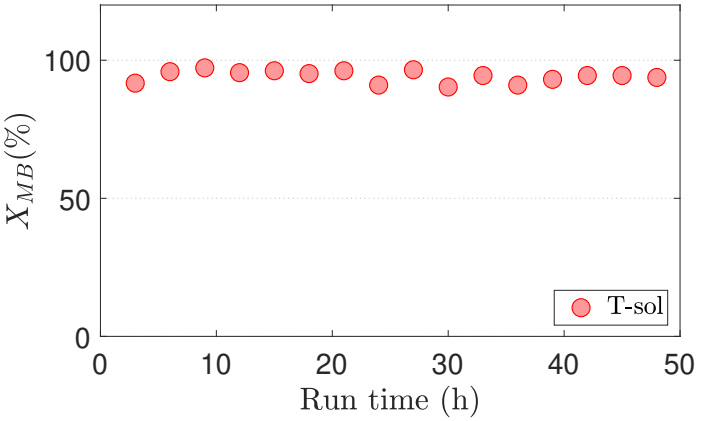

Figure 9: Stability test over a microreactor coated with 0.07 mg/cm^2 of T-sol catalyst (flow rate: 1 ml/h; C_{MB0}: 4 ppm).

4 Conclusions

A novel scalable microfluidic device made of polypropylene was manufactured to study the photodegradation of methylene blue. A simple, low-cost manufacturing approach using laser cutting and transmission laser welding methods was used to build the reactor, while inkjet printing was used for deposition of tunable TiO_2 catalyst films on polypropylene substrate. A synthesized TiO_2 dispersed sol and commercial TiO_2 nanopowders were fully dispersed as stable inks to be used in the printing process by means of a modified desktop printer. The entire process of synthesis and printing was carried out through a calcination free route below 100°C. Low-temperature synthesis and inkjet printing methods cut down the process costs and provide the possibility for using a wide range of materials such as polymers in catalysis and coating technologies. The XRD analysis showed the TiO_2 anatase nanostructures for the synthesized sample. The colloidal inks yielded good droplets, and the layers were uniformly printed onto the substrate. The microreactor showed promising performance and durability for the MB degradation over a long-term running time. The sample prepared by ultrasonic-assisted hydrolysis of $TiCl_4$ was found to be an active and stable photocatalyst. Whilst the printed layers showed sufficient stability during reaction runs, they might need to be more effectively immobilized for rigorous reaction conditions. Surface treatment methods are viable options to enhance the surface adhesive bonding. Furthermore, employing thermally stable polymers such as polyamides would be a research target due to higher resistance to thermal treatments.

Acknowledgement

This work is supported by the European Regional Development Fund through Low Carbon Eco-Innovatory (LCEI) project Grant 22R15P00045, in partnership with CAL International Ltd. The authors thank Dr. Richard Potter for help with XRD measurements, Mr. Dave

Atkinson with SEM analysis, and Mr Oguzhan Der for help with the laser welding procedure.

Supporting Information Available

This will usually read something like: "Experimental procedures and characterization data for all new compounds. The class will automatically add a sentence pointing to the information on-line: This material is available free of charge via the Internet at http://pubs.acs.org/.

References

(1) Yu, J.; Zhao, X.; Zhao, Q. *Thin Solid Films* **2000**, *379*, 7–14.

(2) Fox, M. Anne.; Dulay, M. T. *Chem. Rev.* **1993**, *93*, 341–357.

(3) Linsebigler, A. L.; Lu, G.; Yates, J. T. *Chem. Rev.* **1995**, *95*, 735–758.

(4) Ding, Z.; Lu, G. Q.; Greenfield, P. F. *J. Phys. Chem. B* **2002**, *104*, 4815–4820.

(5) Černá, M.; Veselý, M.; Dzik, P.; Guillard, C.; Puzenat, E.; Lepičová, M. *Appl. Catal., B* **2013**, *138-139*, 84–94.

(6) Fujishima, A.; Rao, T. N.; Tryk, D. A. *J. Photochem. Photobiol., C* **2000**, *1*, 1–21.

(7) Castedo, A.; Mendoza, E.; Angurell, I.; Llorca, J. *Catal. Today* **2016**, *273*, 106–111.

(8) Yu, J.; Yu, J. C.; Ho, W.; Jiang, Z. *New J. Chem.* **2002**, *26*, 607–613.

(9) Bernacka-Wojcik, I.; Wojcik, P. J.; Aguas, H.; Fortunato, E.; Martins, R. *J. Colloid Interface Sci.* **2016**, *465*, 208–214.

(10) Sangchay, W. *Adv. Mater. Res.* **2012**, *626*, 329–333.

(11) Zhao, Z.; Fan, J.; Liu, S.; Wang, Z. *Chem. Eng. J.* **2009**, *151*, 134–140.

(12) Behdani, B.; Monjezi, S.; Carey, M. J.; Weldon, C. G.; Zhang, J.; Wang, C.; Park, J. *Biomicrofluidics* **2018**, *12*, 051503–26.

(13) Taboada, E.; Angurell, I.; Llorca, J. *J. Catal.* **2014**, *309*, 460–467.

(14) Li, S.; Dong, Y.; Guo, M. *Appl. Surf. Sci.* **2012**, *258*, 8015–8018.

(15) Zhan, S.; Chen, D.; Jiao, X.; Song, Y. *Chem. Commun.* **2007**, 2043–2045.

(16) Bharathan, J.; Yang, Y. *Appl. Phys. Lett.* **1998**, *72*, 2660–2662.

(17) Raut, N. C.; Al-Shamery, K. *Journal of Materials Chemistry C* **2018**, *6*, 1618–1641.

(18) Cooley, P.; Wallace, D.; Antohe, B. *J. Assoc. Lab. Autom.* **2002**, *7*, 33–39.

(19) Calvert, P. *Chem. Mater.* **2001**, *13*, 3299–3305.

(20) Dzik, P.; Veselý, M.; Kete, M.; Pavlica, E.; Štangar, U. L.; Neumann-Spallart, M. *ACS Appl. Mater. Interfaces* **2015**, *7*, 16177–16190.

(21) Liu, X.; Tarn, T. J.; Huang, F.; Fan, J. *Particuology* **2015**, *19*, 1–13.

(22) Wu, W. *Nanoscale* **2017**, *9*, 7342–7372.

(23) Cook, B.; Liu, Q.; Butler, J.; Smith, K.; Shi, K.; Ewing, D.; Casper, M.; Stramel, A.; Elliot, A.; Wu, J. *ACS Appl. Mater. Interfaces* **2018**, *10*, 873–879.

(24) Cummins, G.; Desmulliez, M. P. *Circuit World* **2012**, *38*, 193–213.

(25) Waasdorp, R.; Van Den Heuvel, O.; Versluis, F.; Hajee, B.; Ghatkesar, M. K. *RSC Adv.* **2018**, *8*, 14765–14774.

(26) Mahbubul, I. M.; Saidur, R.; Amalina, M. A. *Int. J. Heat Mass Transf.* **2012**, *55*, 874–885.

(27) Mueller, S.; Llewellin, E. W.; Mader, H. M. *Proc. R. Soc. A Math. Phys. Eng. Sci.* **2010**, *466*, 1201–1228.

(28) Derby, B. *Annu. Rev. Mater. Res.* **2010**, *40*, 395–414.

(29) Ma, S.; Ribeiro, F.; Powell, K.; Lutian, J.; Møller, C.; Large, T.; Holbery, J. *ACS Appl. Mater. Interfaces* **2015**, *7*, 21628–21633.

(30) Shin, S.-H.; Park, D. H.; Jung, J.-Y.; Lee, M. H.; Nah, J. *ACS Appl. Mater. Interfaces* **2017**, *9*, 9233–9238.

(31) Brisse, R.; Faddoul, R.; Bourgeteau, T.; Tondelier, D.; Leroy, J.; Campidelli, S.; Berthelot, T.; Geffroy, B.; Jousselme, B. *ACS Appl. Mater. Interfaces* **2017**, *9*, 2369–2377.

(32) Li, Y.; Lan, L.; Sun, S.; Lin, Z.; Gao, P.; Song, W.; Song, E.; Zhang, P.; Peng, J. *ACS Appl. Mater. Interfaces* **2017**, *9*, 8194–8200.

(33) Sundriyal, P.; Bhattacharya, S. *ACS Appl. Mater. Interfaces* **2017**, *9*, 38507–38521.

(34) Liu, Y.; Miao, X.; Fang, J.; Zhang, X.; Chen, S.; Li, W.; Feng, W.; Chen, Y.; Wang, W.; Zhang, Y. *ACS Appl. Mater. Interfaces* **2016**, *8*, 5251–5260.

(35) Siebert, M.; Zimmermann, R. R.; Armbrüster, M.; Dittmeyer, R. *ChemCatChem* **2017**, *9*, 3733–3742.

(36) Mogalicherla, A. K.; Lee, S.; Pfeifer, P.; Dittmeyer, R. *Microfluid. Nanofluid.* **2014**, *16*, 655–666.

(37) Hynek, J.; Kalousek, V.; Žouželka, R.; Bezdička, P.; Dzik, P.; Rathouský, J.; Demel, J.; Lang, K. *Langmuir* **2014**, *30*, 380–386.

(38) Dzik, P.; Morozová, M.; Kluso, P.; Veselý, M. *J. Adv. Oxid. Technol.* **2012**, *15*, 89–97.

(39) Fasaki, I.; Siamos, K.; Arin, M.; Lommens, P.; Van Driessche, I.; Hopkins, S. C.; Glowacki, B. A.; Arabatzis, I. *Appl. Catal., A* **2012**, *411-412*, 60–69.

(40) Arin, M.; Lommens, P.; Avci, N.; Hopkins, S. C.; De Buysser, K.; Arabatzis, I. M.; Fasaki, I.; Poelman, D.; Van Driessche, I. *J. Eur. Ceram. Soc.* **2011**, *31*, 1067–1074.

(41) Watté, J.; Lommens, P.; Pollefeyt, G.; Meire, M.; De Buysser, K.; Van Driessche, I. *ACS Appl. Mater. Interfaces* **2016**, *8*, 13027–13036.

(42) Homola, T.; Dzik, P.; Veselý, M.; Kelar, J.; Černák, M.; Weiter, M. *ACS Appl. Mater. Interfaces* **2016**, *8*, 33562–33571.

(43) Watté, J.; Van Zele, M.; De Buysser, K.; Van Driessche, I. *Coatings* **2019**, *8*, 131–139.

(44) Der, O.; Marengo, M.; Bertola, V. *J. Heat Transfer* **2019**, *141*, 0918081–8.

(45) Ghorbel, E.; Casalino, G.; Abed, S. *Mater. Des.* **2009**, *30*, 2745–2751.

(46) Der, O.; Marengo, M.; Bertola, V. A Low Cost, Flexible Pulsating Heat Pipe Technology. 3rd Thermal and Fluids Engineering Conference (TFEC). Fort Lauderdale, FL, USA, 2018; pp 321–327.

(47) Patterson, A. L. *Phys. Rev.* **1939**, *56*, 978–982.

(48) Addamo, M.; Augugliaro, V.; Di Paola, A.; García-López, E.; Loddo, V.; Marcì, G.; Molinari, R.; Palmisano, L.; Schiavello, M. *J. Phys. Chem. B* **2004**, *108*, 3303–3310.

(49) Xianzhi, F. U.; Clark, L. A.; Yang, Q.; Anderson, M. A. *Environ. Sci. Technol.* **1996**, *30*, 647–653.

(50) Padrón-Hernández, W. Y.; Ceballos-Chuc, M. C.; Pourjafari, D.; Oskam, G.; Tinoco, J. C.; Martínez-López, A. G.; Rodríguez-Gattorno, G. *Mater. Sci. Semicond. Process.* **2018**, *81*, 75–81.

(51) Gebauer, J. S.; Mackert, V.; Ognjanović, S.; Winterer, M. *J. Colloid Interface Sci.* **2018**, *526*, 400–409.

(52) Van Osch, T. H.; Perelaer, J.; De Laat, A. W.; Schubert, U. S. *Adv. Mater.* **2008**, *20*, 343–345.

(53) Zhang, T.; Oyama, T.; Aoshima, A.; Hidaka, H.; Zhao, J.; Serpone, N. *J. Photochem. Photobiol., A* **2001**, *140*, 163–172.

(54) Sampaio, M. J.; Silva, C. G.; Silva, A. M.; Vilar, V. J.; Boaventura, R. A.; Faria, J. L. *Chem. Eng. J.* **2013**, *224*, 32–38.

(55) Di Paola, A.; Bellardita, M.; Ceccato, R.; Palmisano, L.; Parrino, F. *J. Phys. Chem. C* **2009**, *113*, 15166–15174.

Graphical TOC Entry